MNRAS **000**, 1–13 (2016) Preprint 10 June 2016 Compiled using MNRAS LATEX style file v3.0

A critical look at the merger scenario to explain multiple populations and rotation in iron-complex globular clusters

Elena Gavagnin[1⋆], Michela Mapelli[2] and George Lake[1]
[1]*Institute for Computational Science, Centre for Theoretical Astrophysics and Cosmology, Universität Zürich, Winterthurerstrasse 190, CH-8057 Zürich, Switzerland*
[2]*INAF-Osservatorio Astronomico di Padova, Vicolo dell'Osservatorio 5, I–35122, Padova, Italy*

arXiv:1606.02743v1 [astro-ph.GA] 8 Jun 2016

ABSTRACT

Merging has been proposed to explain multiple populations in globular clusters (GCs) where there is a spread in iron abundance (hereafter, iron-complex GCs). By means of N-body simulations, we investigate if merging is consistent with the observations of sub-populations and rotation in iron-complex GCs. The key parameters are the initial mass and density ratios of the progenitors. When densities are similar, the more massive progenitor dominates the central part of the merger remnant and the less massive progenitor forms an extended rotating population. The low-mass progenitor can become the majority population in the central regions of the merger remnant only if its initial density is higher by roughly the mass ratio. To match the radial distribution of multiple populations in two iron-complex GCs (ω Cen and NGC 1851), the less massive progenitor needs to be four times as dense as the larger one. Our merger remnants show solid-body rotation in the inner parts, becoming differential in the outer parts. Rotation velocity V and ellipticity ε are in agreement with models for oblate rotators with isotropic dispersion. We discuss several kinematic signatures of a merger with a denser lower mass progenitor that can be tested with future observations.

Key words: Galaxy: globular clusters - stars: kinematics and dynamics - methods: numerical - galaxies: star clusters

1 INTRODUCTION

Over a quarter of the objects in Messier's catalog are globular clusters (GCs), yet we still do not know how they were formed. For many decades GCs were described as stellar systems with homogeneous chemical composition and no age spread, despite early data showing multiple populations in M22 and ω Cen (Geyer 1967; Canon & Stobie 1973; Harris 1974; Freeman & Rodgers 1975; Hesser & Bell 1980).

Hubble Space Telescope data show a clear bifurcation of colour in the main sequence (MS) of ω Cen (Anderson 1997), with more recent data showing at least four distinct red giant branches (RGBs, Lee et al. 1999; Pancino et al. 2000). Currently, most observed GCs show signatures of multiple populations, both in the Milky Way (Gratton et al. 2004; Carretta et al. 2007; Kayser et al. 2008; Anderson et al. 2009; Carretta et al. 2009b, 2010a; Carretta 2015; Pancino et al. 2010; Milone et al. 2010, 2012, 2013) and in the Magellanic Clouds (Milone et al. 2008).

Most GCs contain stars with similar heavy-element abundances (especially [Fe/H]), but large (>0.5 dex) star-to-star abundance variations for elements lighter than Si (e.g. Cohen 1978; Peterson 1980; Sneden et al. 1991; Kraft et al. 1992; Gratton et al. 2001; Carretta et al. 2009b; Johnson et al. 2015). Moreover, the variations of light-element abundances are anti-correlated with one another (e.g. the O−Na anti-correlation, Gratton et al. 2001). This phenomenology is generally considered to be due to internal enrichment by proton capture H-burning reactions at high temperature (e.g. Gratton et al. 2004).

A minority of GCs also show significant Fe abundance variations. In particular, ω Cen (Norris & Da Costa 1995; Lee et al. 1999; Bellini et al. 2010; D'Orazi et al. 2011; Pancino et al. 2011), M22 (Hesser et al. 1977; Marino et al. 2009; Lee 2015), M2 (Piotto et al. 2012; Lardo et al. 2013; Milone et al. 2015), M54 (Sarajedini & Layden 1995; Bellazzini et al. 2008; Carretta et al. 2010b), NGC 1851 (Yong & Grundahl 2008; Milone et al. 2009; Carretta et al. 2010c, 2011), NGC 5286 (Nataf et al. 2013; Marino et al. 2015), NGC 5824 (Saviane et al. 2012; Da Costa et al. 2014), Terzan 5 (Ferraro et al. 2009; Massari et al. 2014) and M19 (Johnson et al. 2015) are labelled as 'iron-complex' GCs, because

⋆ E-mail: gavagnin@physik.uzh.ch

© 2016 The Authors

they have (i) a spread[1] in [Fe/H] exceeding ~ 0.10 dex, (ii) multiple photometric sequences, and (iii) a significant abundance spread for both light and heavy elements (Johnson et al. 2015). Iron-complex GCs differ from other GCs in several ways. In most GCs, the stellar population showing no enrichment by proton capture accounts for about one third of the total GC mass, with little spread among GCs (Carretta et al. 2009a). In contrast, in the iron-complex GCs, the ratio between the metal-poor and the metal-rich population changes from cluster to cluster. For example, in M19 the metal-poor component is ~ 50 % of the entire population (Johnson et al. 2015), whereas ~ 96 % of spectroscopically studied stars in M2 belong to the metal-poor component (Milone et al. 2015). Moreover, in the vast majority of GCs, the proton-capture enriched population is more radially concentrated than the most numerous one. In the iron-complex GCs the metal-poor population can be either more concentrated (ω Cen, Bellini et al. 2009) or less concentrated (NGC 1851, Carretta et al. 2011) than the metal-rich one.

Several theoretical models have been proposed to explain the multiple populations (Bastian et al. 2013; see Renzini 2008 for a review). A first class of models appeals to multiple star-formation events. After first population stars form out of pristine, metal-poor gas, the second population of stars might form from either the ejecta of asymptotic giant branch (AGB) stars (D'Ercole et al. 2008) or fast rotating massive stars (FRMS, Decressin et al. 2007). In the 'AGB scenario', winds and supernovae (SNe) of the first population evacuate the residual gas. After ~ 30 Myr, low-velocity winds from AGBs enriched in He and s-process elements start accumulating at the centre and form the second population. However, the predicted mass of the second population is an order of magnitude lower than what is observed, requiring a top-heavy first population initial mass function and an unusually efficient second population star formation.

A second model, called the 'early disc accretion model' (Bastian et al. 2013), proposes that the two populations formed during the same star formation episode, but underwent different chemical enrichment. This model requires very fast mass segregation and gas evaporation. With rapid mass segregation, the most massive stars sink to the centre where high-mass stars in interacting binaries eject the primary's He-enriched envelope. This material pollutes the circumstellar discs of low mass stars that are still accreting, so they will grow in mass thanks to these ejecta from more massive (but still same-generation) stars. The main drawbacks of this model are disc lifetime and uniformity of enrichment. Even if circumstellar discs survive for the required $5-10$ Myr (De Marchi et al. 2013), the "rainfall" of enriched material onto them is unlikely to be uniform (Kruijssen 2014).

All the aforementioned scenarios are aimed to explain multiple populations with no or negligible iron spread, while they fail to reproduce the [Fe/H] variations observed in the iron-complex GCs. So far, the only proposed scenario that can naturally account for a metallicity spread is the merger between GCs (Sugimoto & Makino 1989; Makino et al. 1991; van den Bergh 1996; Amaro-Seoane et al. 2013; Pasquato & Chung 2016). In this scenario, the different metallicities are signatures of the progenitors and can be used as a tag to make predictions about the distribution and dynamics within the final merger remnant. Iron abundance is, in this respect, a good tag to identify uniquely the different populations.

The merger scenario might be consistent with the oldest metal-rich stars in ω Cen being a few Gyrs older than the oldest metal-poor stars (Villanova et al. 2014), a circumstance that is against the predictions of self-enrichment scenarios. Furthermore, a merger can explain the kinematical differences in the velocity dispersion of the calcium-weak and calcium-strong RGB stars in M22 (Lee 2015). The merger scenario has been proposed also for NGC 1851, where the most metal-rich population is less concentrated than the metal-poor one (van den Bergh 1996; Carretta et al. 2010c, 2011; Bekki & Yong 2012).

Another advantage of the merger scenario is that it can account for signatures of rotation in GCs, which have been observed in several GCs with multiple populations, both with (e.g. ω Cen, M2, M22, M54, NGC1851, Pancino et al. 2007; Lee 2015; Pryor et al. 1986; Kimmig et al. 2015; Bellazzini et al. 2012; Lardo et al. 2015) and without (e.g. Fabricius et al. 2014) a metallicity spread. If the two progenitors have non-zero relative orbital angular momentum, the merger remnant will likely preserve a signature of rotation in the merger plane. However, there is no evidence that GCs with a metallicity spread (the best-candidate merger remnants) have systematically higher rotation than the other GCs. Moreover, other physical mechanisms can account for rotation in GCs (e.g. Mastrobuono-Battisti & Perets 2013; Vesperini et al. 2014; Bianchini et al. 2015).

The main problem for the merger scenario is that two GCs are expected to merge only if their relative velocity is smaller than (or of the same order of magnitude as) their velocity dispersion. The largest GC in the galaxy, ω Cen, has a dispersion of ~ 8 km s^{-1}, with typical values being $\sim 4-6$ km s^{-1}. The relative velocities of current GCs in the Milky Way halo are at least one order of magnitude larger than these values. This means that a merger between two GCs that are in the halo of our galaxy is extremely unlikely. Two GCs will have a sufficiently low relative velocity to merge only if they formed in a small dwarf galaxy or in the same molecular cloud. However, if the two progenitor clusters formed in the same molecular cloud and merged slightly after their formation, it is difficult to explain why the two populations have a different proton-capture enrichment and even a different metallicity. Therefore, GCs in small dwarf galaxies represent the most likely scenario where GC mergers will produce clusters that have a spread in metallicity.

We take a critical approach to the merging scenario by examining how the initial mass and density ratios of the progenitors affect the distribution and concentration of the subpopulations in the remnant (Section 3.1). Moreover, we also examine the rotation signature of the merger product and we show that the profile of rotation is related to the initial density ratio of the progenitors (Section 3.2). In the event of equal-mass mergers, we expect that the denser initial progenitor will be more centrally concentrated in the remnant. In the case of unequal-mass mergers, the more massive progenitor will be closer to the centre than the less massive

[1] Recent studies highlight the possibility that the [Fe/H] spread is spurious, at least in some GCs (e.g. M22, Mucciarelli et al. 2015), because spectroscopically derived Fe abundances might be inaccurate due to non-local thermodynamical equilibrium effects.

progenitor and hence be more concentrated. We examine how the density ratio can counter the mass ratio.

This paper is organised as follows. In Section 2, we describe the numerical tools and the initial conditions adopted. In Section 3, we present the main results of this work. Section 4 is dedicated to the discussion and conclusions.

2 METHODS AND SIMULATIONS

We used the STARLAB public software environment (Portegies Zwart et al. 2001) ported to GPUs (Gaburov et al. 2009) to run the simulations. To investigate the role of the relative masses and densities of the progenitors, we performed a grid of simulations varying the mass ratio, i.e. M_1/M_2 (where M_1 is the mass of GC1 and M_2 is the mass of GC2) and the density ratio, i.e. ρ_1/ρ_2 (where ρ_1 and ρ_2 are the densities measured at the virial radius of GC1 and GC2, respectively).

We consider mass ratios of 1, 2, 4, with density ratios of 0.25, 0.5, 1, 2, 4. The range is motivated by the ratio of the populations in GCs (Johnson et al. 2015; Milone et al. 2015) and the absence of strong correlations between luminosity and density in present-day GCs (Harris 1996). The GCs are modelled as non-rotating spherical King profiles (King 1966) with central dimensionless potential $W_0 = 5$ (this sets the core radius $R_c = 0.41 R_V$). The second GC (GC2) is always composed of 20 000 particles of equal mass $m_* = 5\,M_\odot$ for a total mass of 10^5 $M_\odot$. Its virial radius $R_V = 4$ pc. The first GC (GC1) is varied to set the mass ratio and density ratio. To double (or quadruple the mass) of GC1, we double (or quadruple) the number of particles.

The density ratio is set by adjusting the virial radius of GC1, e.g. in the run $M2\rho1$ the GC1 has twice the mass as GC2 and R_V of GC1 is $\sim 1.26\times$ larger than the one of GC2, so that the density ratio between the two clusters is 1. We note that, assuming a fixed value for W_0, the density ratio is the same at every fiducial radius, i.e. the core radius (R_c), the tidal radius (R_t) and the virial radius (R_V).

To prevent strong encounters and binary formation, we adopt a gravitational softening $\varepsilon = 0.1 R_V$ of the progenitor with the smallest radius. The initial binary fraction is zero and binaries do not form with this softening. We omit stellar and binary evolution to minimise the amount of free parameters in these models. Stellar and binary evolution might affect the structural properties of GCs (Chernoff & Weinberg 1990; Mapelli et al. 2013; Mapelli & Bressan 2013; Trani et al. 2014; Gieles 2013; Sippel et al. 2012) and will be considered in a follow up study. Stars initially belonging to each of the two progenitors are "tagged" with a different metallicity flag. Initial conditions (ICs) are summarised in Table 1.

The two GCs are initially set on a parabolic orbit. To define the parabolic orbit we fixed the minimum encounter distance (in the point-mass assumption), i.e. the pericentre r_{peri}, to be half the sum of the virial radii of the two progenitors GC1, GC2 [$r_{peri} = 0.5\,(R_{V1} + R_{V2})$]. The initial distance D between the progenitors is four times the maximum value between $R_{t,1}$ and $R_{t,2}$, where $R_{t,1}$ and $R_{t,2}$ indicate the tidal radius of GC1 and GC2, respectively. The initial relative velocity is then calculated as the escape velocity at the initial position.

We choose a parabolic orbit because it is a representative case for mergers (Alladin 1965; White 1978). Hyperbolic encounters (with relative velocity much larger than the GC velocity dispersion) are the most common, as the phase space for encounters increases with the cube of the velocity of encounter and the cube of the impact parameter. However, the probability of merging encounters is sharply truncated (by failure to merge) when the orbits become very weakly hyperbolic. In contrast, the two GCs will merge on a shorter timescale if they are on a bound orbit, but bound orbits are associated with smaller values of the velocity. As we mentioned in the introduction, the main drawback of the merger scenario is that the observed relative velocities between GCs are generally larger than the value needed for a merger to be successful. Thus, we consider bound orbits very unlikely. In summary, a parabolic orbit is representative of the most likely orbits leading to a merger.

The half-mass relaxation time is (Spitzer 1987)

$$t_{rlx} \sim 3\times10^8 \mathrm{yr} \left(\frac{M}{10^5\,M_\odot}\right)^{1/2} \left(\frac{R_{hm}}{3\,\mathrm{pc}}\right)^{3/2} \left(\frac{m}{5\,M_\odot}\right)^{-1} \left(\frac{\ln\Lambda}{3}\right)^{-1}, \quad (1)$$

where R_{hm} is the initial half-mass radius, M the total mass, m is the particle mass and $\ln\Lambda$ is the Coulomb logarithm (set here by the system size and gravitational softening). For our progenitors, the relaxation timescales are between 400 Myr and 1.7 Gyr. The initial crossing time at the virial radius in the equal mass, equal density progenitors is ~ 0.4 Myr and scales as $\rho^{-1/2}$. We run our simulations for 550 Myr. This is less than one half-mass relaxation timescale characteristic of the merger product in all cases, but two-body encounters have likely contributed to isotropising the velocities in the remnant.

3 RESULTS

We examine the relative concentration and rotation of the two different populations in the merger remnant.

3.1 Relative Concentration

We plot the relative concentration using normalised density profiles of the sub-populations (i.e. each density profile is divided by its progenitor's mass). Figure 1 shows the density profile of GC1 and GC2 in green and in magenta respectively (where $M_{GC1} \geqslant M_{GC2}$).

We plot the profiles of nine selected runs. The profiles are at time ~ 550 Myr since the beginning of the simulation. We see that the final density profiles of the merger remnants are consistent with a single King model profile, although the two populations have different densities in the central regions. Depending on the run, we note that at small radii the normalised density of GC1 members can be higher than that of GC2 members or *viceversa*. This suggests that the initial mass and density ratios affect the *relative* central density of the two populations in the final merger remnant (Figure 1). Despite the normalisation to the progenitor's mass, at large radii one curve is below the other in several panels. For example, in several plots of Figure 1 the magenta curve is below the green one (see especially the bottom right panel:

Table 1. Initial conditions of the simulations. Run (column 1): identifying name of the run, 'M' stands for mass ratio ($M1/M2$), 'ρ' for density ratio (ρ_1/ρ_2), both followed by the values assumed, e.g. M4ρ0.25, means mass ratio = 4, density ratio = 0.25; column 2: progenitor identifier; N (column 3): number of particles; M (column 4): total mass of the progenitor; R_V (column 6): virial radius; D (column 7): initial distance between the progenitors' centres of mass; r_{peri} (column 9): orbital pericentre; V (column 10): initial relative velocity.

Run		N	M [$M_\odot$]	R_V [pc]	D [pc]	r_{peri} [pc]	V [km s^{-1}]
	GC2	20k	10^5	4			
M1ρ0.25	GC1	20k	10^5	6.34	111.58	5.17	5.59
M1ρ0.50	GC1	20k	10^5	5.03	88.5	4.51	6.27
M1ρ1	GC1	20k	10^5	4	70.4	4	7.03
M1ρ2	GC1	20k	10^5	3.17	70.4	3.59	7.03
M1ρ4	GC1	20k	10^5	2.52	70.4	3.26	7.03
M2ρ0.25	GC1	40k	$2\cdot10^5$	8	140.8	6	6.09
M2ρ0.50	GC1	40k	$2\cdot10^5$	6.34	111.58	5.17	6.84
M2ρ1	GC1	40k	$2\cdot10^5$	5.03	88.5	4.51	7.68
M2ρ2	GC1	40k	$2\cdot10^5$	4	70.4	4	8.61
M2ρ4	GC1	40k	$2\cdot10^5$	3.17	70.4	3.59	8.61
M4ρ0.25	GC1	80k	$4\cdot10^5$	10	176	7	7.03
M4ρ0.50	GC1	80k	$4\cdot10^5$	8	140.8	6	7.86
M4ρ1	GC1	80k	$4\cdot10^5$	6.34	111.58	5.17	8.83
M4ρ2	GC1	80k	$4\cdot10^5$	5.03	88.5	4.51	9.92
M4ρ4	GC1	80k	$4\cdot10^5$	4	70.4	4	11.12

since the profiles are normalised to the mass of the progenitors, this is a clear signature of mass loss during the merging process).

Figure 2 is a colour map of the relative concentration of the two progenitors, defined as '$\log(R_{hm2}/R_{hm1})$', i.e. the logarithm of the ratio between the half-mass radius of GC2 and GC1, in the initial conditions and at the end of the simulations, for the whole grid of runs. The plot on the left-hand side in Figure 2 shows the ratio between the half-mass radius of GC2 and GC1 in the ICs, the plot on the right-hand side shows the same quantity after the merger. From the right panel in Figure 2, we see that when the initial densities are equal, the more massive progenitor dominates the central part of the merger remnant and the less massive progenitor is more extended in the merger remnant. If the progenitors have equal masses, the denser progenitor is more concentrated in the remnant. To compensate for an unequal mass ratio, the less massive progenitor must have a density larger by roughly the factor by which its mass is lower. If the smaller mass progenitor is $1/A$ as massive, its initial density must be A times greater or alternatively, its radius must be $A^{-2/3}$ as large as the more massive one.

In Figure 3 we compare the number ratio of sub-populations (N_2/N_1) in our simulated GCs with the observations. Specifically, we plot the ratio of the minority (N_2) to the majority (N_1) population against the radial distance from the centre, normalised to the half-mass (or half-light) radius. Observational data of three GCs are compared with our simulations: in ω Cen the metal-rich population is the most centrally concentrated and is the minority population (Bellini et al. 2009), in NGC 1851 (Carretta et al. 2011) and M22 (Carretta et al. 2011) the metal-poor population is the more centrally concentrated (note that crowding prevents observing the very central regions of NGC 1851). In M22 the metal-rich population is the minority, while in NGC 1851 the metal-poor population is the minority.

The two runs shown in Figure 3 (M2ρ0.25 and M2ρ1) were not tuned to reproduce the observations, but follow the same trend as the data. In our simulations, the metallicity is only a tag: in the top panel of Figure 3 we use the same model (with a denser minority population) to match cases where the minority population is more concentrated, but the minority population is metal rich in ω Cen and metal poor in NGC 1851. We adopt a different progenitors model (with equal density) for M 22, where the minority population (metal-rich) is less concentrated.

3.2 Rotation

Rotation is observed in nearby GCs (Anderson & King 2003; van den Bosch et al. 2006; Bellazzini et al. 2012; Lardo et al. 2015; Fabricius et al. 2014), which can arise from a variety

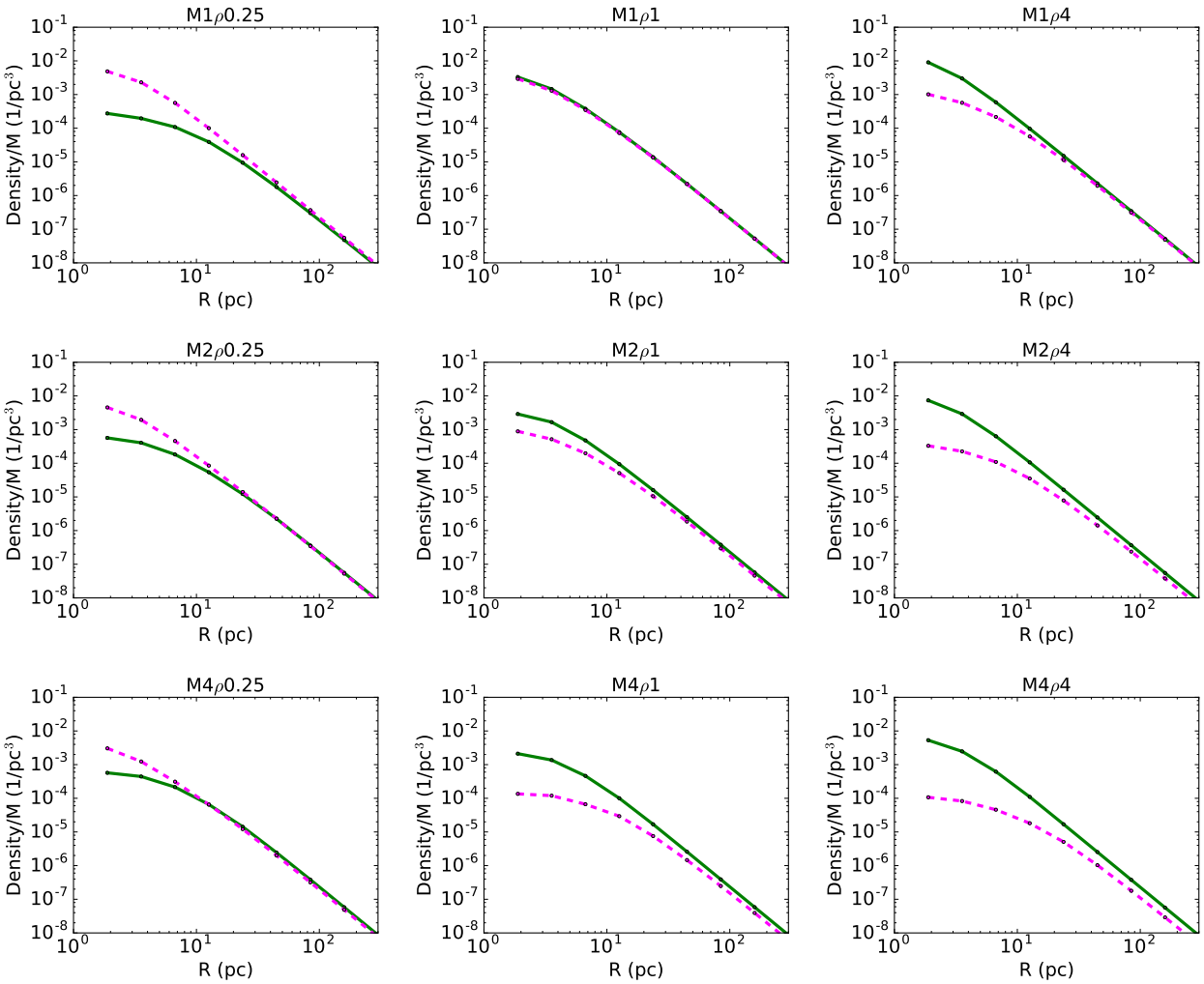

Figure 1. Normalised density profiles of the two populations in the final merger remnant. Note that the profiles all look like smooth King models. Solid green line refers to GC1, dashed magenta line to GC2. Each profile has been normalised by the mass of the associated progenitor. The codename on the top of each plot refers to the run considered: 'M' stands for mass ratio M_1/M_2 followed by its value, 'ρ' for density ratio ρ_1/ρ_2 followed by its value. From top to bottom the mass ratio increases by a factor of 2 every row and from left to right the density ratio increases by a factor of 4 every column.

of mechanisms (Bertin & Varri 2008; Varri & Bertin 2012; Bianchini et al. 2013; Vesperini et al. 2014). While there is no connection demonstrated between rotation and multiple populations, Amaro-Seoane et al. (2013) pointed out that ω Cen, M 22, and NGC 2419 are among the most flattened clusters.

Flattening has been detected in several galactic GCs (White & Shawl 1987; Chen & Chen 2010) and could be explained by several physical factors, such as pressure anisotropy or external tides (van den Bergh 2008). Another possible justification for the flattening is the internal rotation of GCs (Fabricius et al. 2014). A correlation between flattening and iron-complex multiple populations would favour the merger scenario.

In this section, we look at the detailed kinematics of our merger remnants, as a function of mass and density ratios. We want to quantify their amount of rotation and see whether their degree of flattening correlates with rotation.

All of our merger remnants have rotation, as a consequence of the parabolic orbits of their progenitors. In Figs. 4, 5 and 6, we show velocity maps for the complete range of initial mass ratios and the limiting cases of density ratios $\rho_1/\rho_2 = 0.25, 4$. In all cases, we plot line-of-sight velocities for an observer sitting on the mid-plane perpendicular to the rotation axis. For comparison with the observations (Fabricius et al. 2014), we used a Gaussian filter to create the velocity map, progressively zoomed from left to right. Even the largest spatial scales of the final merger state (left-hand columns) show a clear flattening and the two populations have similar properties in configuration and velocity space.

These maps illustrate some important trends: the rotation within 5 pc is generally solid body, it becomes differential at $5-10$ pc, and the rotation is cylindrical everywhere. The similarity of the maps shows that these features are common to all our simulations. Solid-body rotation is the most probable distribution function (maximal entropy) for the relaxed core of a rotating N-body system (Lynden-Bell 1967; Lightman & Shapiro 1978). Observations of clusters also show solid body rotation over most of the half-mass

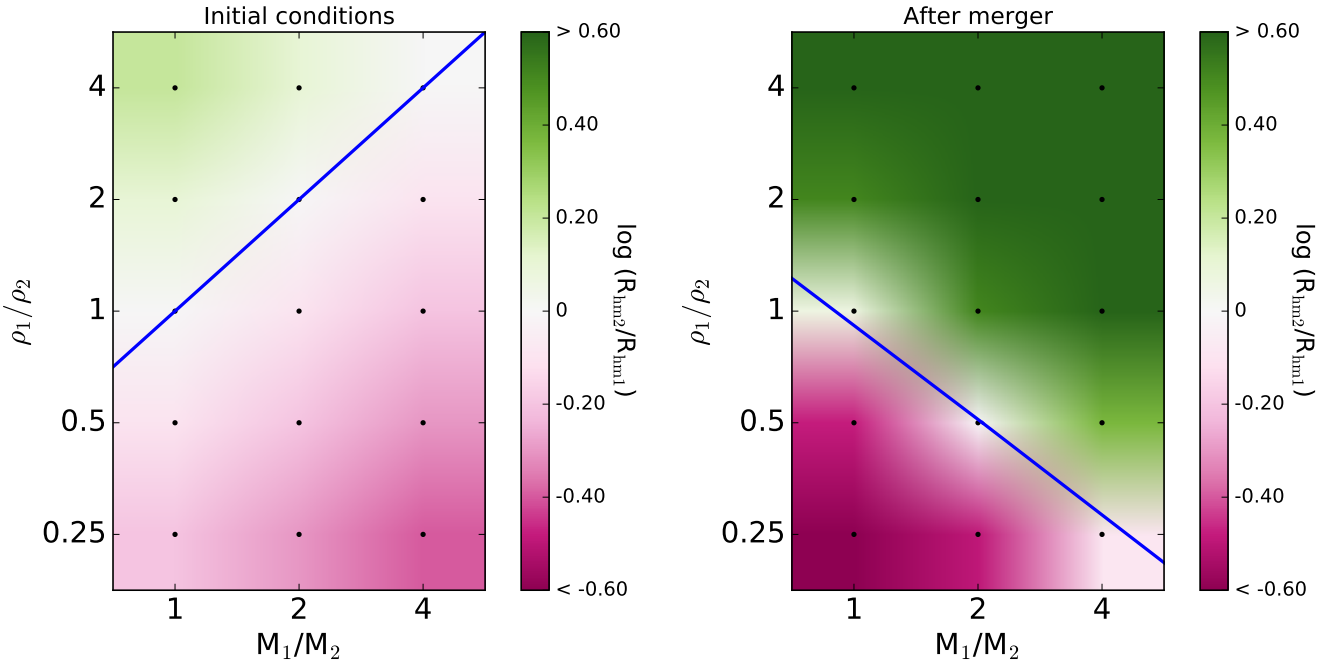

Figure 2. Colour map of initial (left) and final (right) ratio between the half-mass radius of GC2 and GC1 ($\log(R_{hm2}/R_{hm1})$). The $x-$ and $y-$axis are the initial mass ratio and the initial density ratio of the two progenitors. The colour map quantifies the relative concentration of the two populations (in logarithmic scale), meaning the ratio of the two half-mass radii i.e. R_{hm2}/R_{hm1}. If the logarithm of this value is negative (magenta) GC2 is more centrally concentrated in the merger product; if it is positive (green), GC1 is more centrally concentrated. The blue line marks the boundary between where GC1 is more centrally concentrated (green) and the situations where GC2 is more centrally concentrated (magenta). In both plots, the actual data grid at which R_{hm2}/R_{hm1} is evaluated is marked with black dots, the colour map is then smoothed via interpolation in order to highlight the general trend. Note that the $x-$ and $y-$axis are effectively logarithmic.

radius and differential rotation outside (Meylan & Mayor 1986; Bianchini et al. 2013; Fabricius et al. 2014).

Figure 7 shows the line-of-sight rotation profiles of all the simulations for an observer sitting on the rotation plane. As in the velocity maps, we see that the inner rotation is solid-body, then it becomes differential at 5-10 pc. The solid-body rotation region is more extended in the runs with higher mass ratio; the angular momentum of the less massive object is preferentially deposited in the outskirts of the remnant.

At the half mass radius, the merger remnant exhibits solid-body or differential rotation depending on the initial density ratio between the progenitors. In Figure 8, we examine the ratio of the rotation velocity at the half-mass radius to the maximum rotation velocity V_{Rhm}/V_{max}, as a function of density ratio. For equal-mass ratios the quantity V_{Rhm}/V_{max} is almost constant with respect to the density ratio (top panel of Figure 8). Therefore each of these model clusters have transitioned from solid-body to differential rotation by the half mass radius. In contrast, the trend for unequal mass ratios provides an interesting test of the model. When the less massive progenitor is less dense, it deposits its angular momentum in the outer parts. In contrast, small-mass progenitors with larger density burrow into the centre. When the minority population is more concentrated, the rotation curve will peak at roughly the half-mass radius, whereas when the minority population is less concentrated, the peak occurs outside the half-mass radius. Therefore, for unequal-mass ratios, V_{Rhm}/V_{max} decreases for increasing values of the density ratio.

In order to compare the outcomes of our simulations with observations, we study now the $(V/\sigma,\ \varepsilon)$ diagram, which relates the ratio of the rotation velocity V and random motion σ to the ellipticity ε, which measures the flattening.

The expectation for isotropic rotators are derived from the tensor virial theorem (Chandrasekhar 1969). The rotation velocity is the square root of the mass weighted streaming velocity squared. The velocity dispersion is the unordered kinetic energy. If the mass is stratified on concentric similar ellipsoids, the density profile drops out (Roberts 1962; Chandrasekhar & Lebovitz 1962) and the ratio of the ordered kinetic energy to the unordered one (or its square root V/σ) is a function only of the ellipticity ε (Binney 1978). The application to elliptical galaxies is straightforward since V, σ and ε are all nearly constant with radius (Emsellem et al. 2007).

For GCs, ε has a greater variation with radius and V is rising with an asymptote at a radius beyond the observations. Hence, we look at how well 'proxy' and 'measured' rotations relate to one another in the simulated merger remnants. As always with proxies and dimensionless parameters that vary with radius, the results will be mixed.

In Figure 9 we plot the $(V/\sigma,\ \varepsilon)$ diagram, following the prescription of Fabricius et al. (2014) as proxies for V and ε, including both data from our simulations and observed GCs. Fabricius et al. (2014) fit a plane $V(x,y) = ax+by+V_{sys}$ (where V_{sys} is the systemic velocity) to the velocity fields to

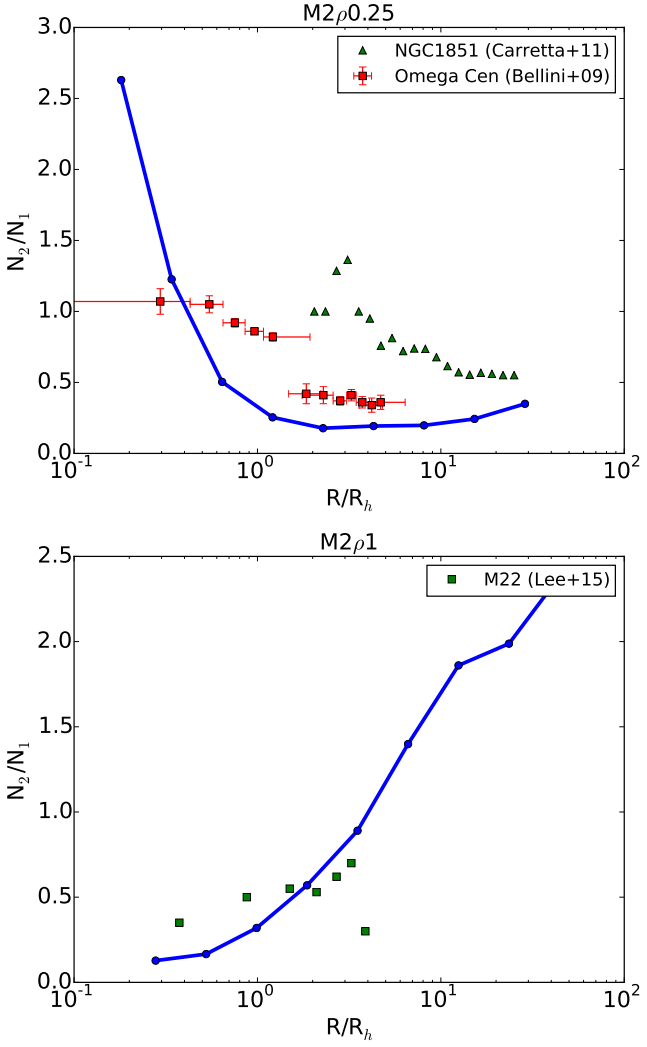

Figure 3. Ratio of the minority (N_2) to the majority (N_1) population versus the radial distance from the centre. The blue solid line indicates our simulated models M2ρ0.25 (top panel) and M2ρ1 (bottom panel). The data points refer to observations (Bellini et al. 2009 for ω Cen, Carretta et al. 2011 for NGC 1851, and Lee 2015 for M 22). N_2/N_1 is normalised to the half-mass radius and to the half-light radius for the simulations and for the observations, respectively.

determine the central velocity gradient, $||\nabla V|| = \sqrt{a^2+b^2}$. They take velocity dispersions σ and half-light radii R_{hl} from Harris (1996) to create a proxy for rotational velocity $\nabla V \cdot R_{hl}$, and find V/σ increasing with ellipticity. In our case, we define V in similar way ($\nabla V \cdot R$) leaving though R as free parameter, with the intent to explore how this proxy for V depends on the radius used to define it. ∇V is also calculated within the radius considered each time. Specifically, in Figure 9 we considered three different values of radius R, that are $R_{\rm hm}$, $R_{\rm hm}/2$, and $R_{\rm hm}/4$. Our choice is justified by Figure 7, where the solid-body rotation shifts to differential rotation at radii varying from $\sim 0.5 R_{\rm hm}$ to $\sim 1.5 R_{\rm hm}$.

σ in our case is just the line-of-sight velocity dispersion. As for the ellipticity, we follow the prescriptions found in Fabricius et al. (2014) and calculate ellipticity values (ε) from the eigenvalues (λ_1, λ_2) of the covariance matrix of stellar positions (within the relevant radial dimension), i.e. $\varepsilon = \sqrt{1-\lambda_2/\lambda_1}$.

Figure 9 shows that the result strongly depends on the choice of radius. The V/σ ratio increases with ellipticity, but ellipticities and V/σ both increase with radius. If we looked at Figure 7, we might guess that something close to $\nabla V \cdot R_{\rm hm}$ would be the best proxy and certainly would not have guessed that the plot using $\nabla V \cdot R_{\rm hm}/4$ would look most like the oblate rotator (dashed line in the plot) and would be most in agreement with the data from Fabricius et al. (2014) . Thus, the choice of rotational velocity in a (V/σ, ε) diagram is not unique[2].

Another possibility is to take as the rotation velocity the maximum rotational velocity. In Figure 10, we plot the ellipticity ε of our simulated merger remnants versus $V_{\rm max}/\sigma$, where $V_{\rm max}$ is the maximum rotational velocity (see Figure 7). The result (shown as star symbols in Figure 10) compares favourably with the oblate rotator curve and observations. Having set the initial orbits to parabolic, the values of ($V_{\rm max}/\sigma$, ε) for the simulated GCs are all in the same portion of the oblate rotators curve. With time, the merger remnants will radiate away angular momentum through two-body encounters (Fall & Frenk 1985). This will make them slide down on the curve to lower ellipticity and V/σ values, closer to the observational data, because rotation and ellipticity will decrease significantly as soon as the system relaxes and the two populations mix completely (velocities will isotropise and angular momentum will diminish).

In Figure 9 and Figure 10, we plot not only the observational sample of Fabricius et al. (2014), whose 11 GCs do not show any significant spread in Fe abundance, but also data of some iron-complex GCs (M 22 and M 54 from Bellazzini et al. 2012, M 2 from Pryor et al. 1986, ω Cen from Bianchini et al. 2013, NGC 1851 from Lardo et al. 2015). To derive the value of $V_{\rm max}/\sigma$ for the iron-complex GCs, we use the double mean velocity amplitude (i.e. $A_{\rm rot}$) which is considered a good representation of $V_{\rm max}$ (Pancino et al. 2007). From the kinematical point of view, the iron-complex GCs for which V/σ and ε are available do not stand out in comparison with the sample of Fabricius et al. (2014).

4 DISCUSSION AND CONCLUSIONS

In this section, we discuss the results of our simulations in light of the observational properties of iron-complex GCs. We focus on GCs with multimodal iron-complex abundances because they have unique tags that can be mapped to possible progenitors.

In the merger scenario, we find that the minority population is less centrally concentrated unless the initial density of the less massive progenitor is greater by more than the mass ratio. In M22, the minority is metal poor and extended. The distribution compares well to equal density progenitors with a mass ratio of 2:1. In ω Cen and NGC1851 the less massive population is more centrally concentrated than the

[2] The proxy for ∇V adopted by Fabricius et al. (2014) would always be higher than the true rotation velocity at the radius R, because it comes from the best linear fit to the velocities within R and the second derivative of V with respect to R is negative (the rotation curve is flattening).

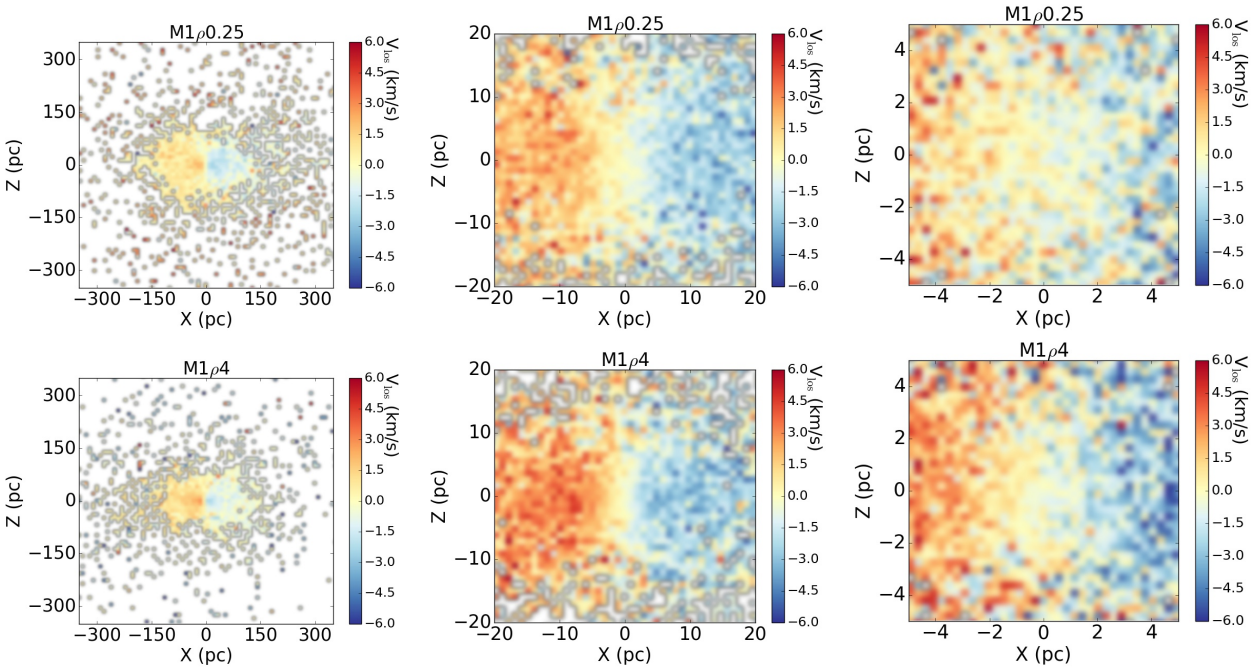

Figure 4. Line-of-sight velocity maps at different scales at t= 550 Myr for the case with equal mass ratio between the progenitors and ρ_1/ρ_2=0.25 (top row), ρ_1/ρ_2=4 (bottom row). From left to right, we zoom in the central parts of the remnant. The largest scales (left-hand columns) show a clear flattening. Examining these colour maps, the rotation within 5 pc is generally solid body (colour is changing), it becomes differential at 5-10 pc (the colour stays constant outside this radius in the rotation plane) and it is cylindrical everywhere (weak or no colour trend vertically). The similarity of all the maps reveals that these are common features of mergers.

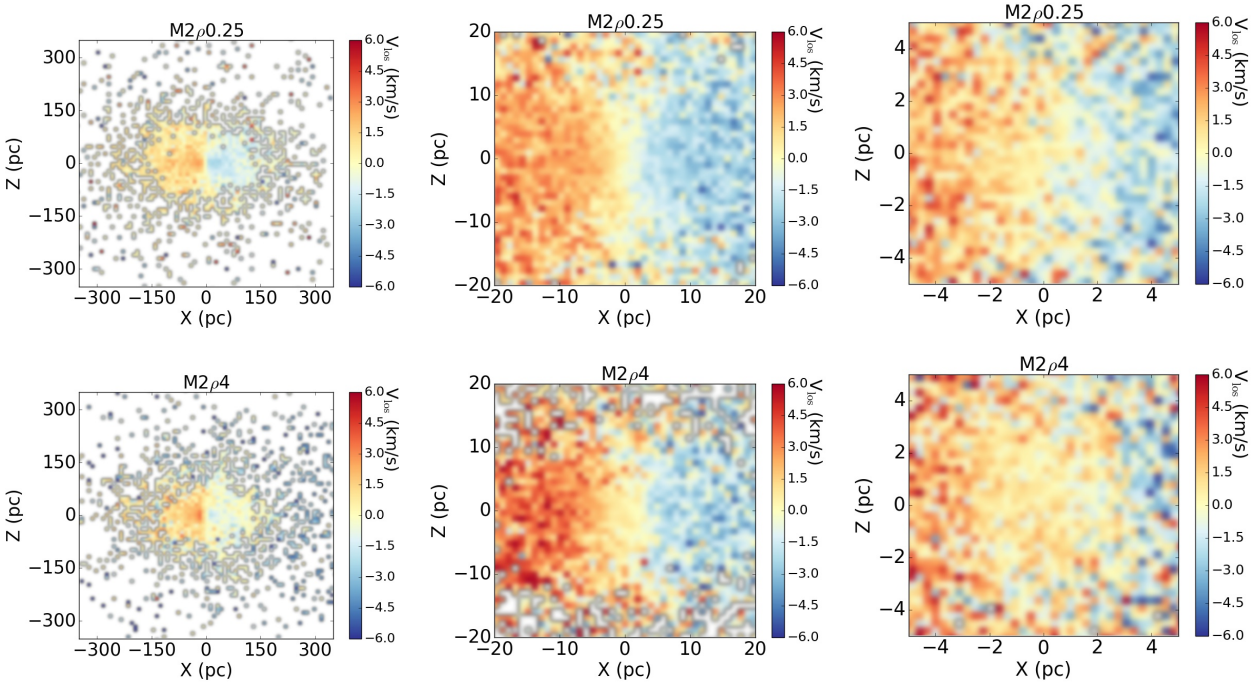

Figure 5. The same as Figure 4, but for the case with 2:1 mass ratio between the progenitors and ρ_1/ρ_2=0.25 (top row), ρ_1/ρ_2=4 (bottom row).

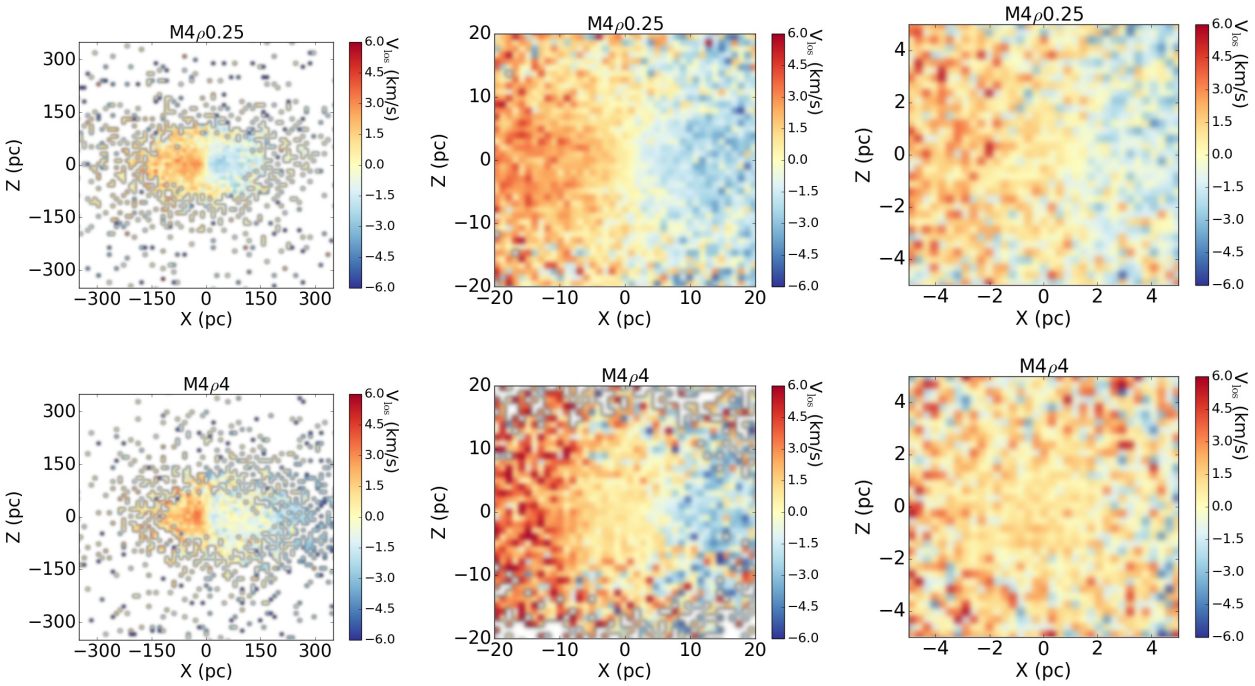

Figure 6. The same as Figure 4, but for the case with 4:1 mass ratio between the progenitors and ρ_1/ρ_2=0.25 (top row), ρ_1/ρ_2=4 (bottom row).

majority population (Bellini et al. 2009). Merging only cares about metallicity if there is a correlation between metallicity and mass or density. The minority is metal rich in ω Cen, while it is metal poor in NGC 1851. In light of our results, this means these GCs can be the result of a merger only if the less massive progenitor was the denser one. These trends are best fit when the mass ratio is 2:1 and the less massive progenitor is four times as dense as the more massive one.

It would be instructive to check with observations whether the less massive progenitors are denser than more massive ones. Figure 11 shows the relation between luminosity (as a proxy for mass) and half-light radius in present-day GCs, from the catalogue of Harris (1996). This figure shows that there is no correlation between luminosity (hence, mass) and size in present-day Milky Way GCs. From this fact, we cannot conclude very dense but small mass progenitors would be common, if merger progenitors were like present-day GCs. However, we also warn that considering present-day GCs as representative of merger progenitors is rather hazardous.

The kinematical signatures of the merger remnant are similar to those observed in GCs. In our simulated remnants: 1) the velocity dispersion is isotropic, 2) the merger product rotates close to solid body in the inner parts, then becomes differential, 3) rotation is cylindrical, 4) at the half mass radius, the merger remnant exhibits solid-body or differential rotation depending on the initial density ratio between the progenitors, 5) the flattening of the remnant is consistent with rotation. Both ε and V vary over radius, so defining appropriate values for a $(V/\sigma,\varepsilon)$ plot is difficult. Different choices move points around in that plot, but the correlation between flattening and rotation in the remnants is similar to the expectations from the tensor virial theorem (Binney 1978).

As we already anticipated in the introduction, the most severe drawback of the merger scenario is that the relative velocity between two clusters must be sufficiently low to merge. Here 'sufficiently low' means that their relative velocity cannot be much larger than their velocity dispersion. The velocity dispersion of GCs is ≈ 3 per cent of the velocity dispersion of stars in the field of our Galaxy. This means that GCs move too fast to merge in our present-day Galaxy.

Several studies propose that a sub-population of GCs were the nuclei of dwarf galaxies, with ω Cen as prototype (Majewski et al. 2000; Carraro & Lia 2000). If one GC were a nucleus, the inspiral of a second GC would create conditions similar to an unequal mass merger.

GCs can sink toward the centre of the host galaxy by dynamical friction. The dynamical friction timescale scales as the inverse of the mass of the GC. Thus, the smaller the GC, the longer it takes for it to sink to the centre by dynamical friction. For example, an object that has a mass of ~ 5 per cent of the total mass of the host galaxy will spiral into the centre by dynamical friction in roughly a dynamical time (Binney & Tremaine 2008).

The smallest dwarf galaxy in the Local Group with GCs is Fornax, with five clusters (Larsen et al. 2012). The most massive among these GCs has not yet sunk into the centre by dynamical friction (Read et al. 2006). Thus, even Fornax failed to promote mergers or create a nucleus from its most massive GC.

The Sagittarius dwarf galaxy is more promising (Gratton et al. 2012). At least five Milky Way GCs are thought to have been part of Sagittarius (Law & Majewski 2010). The velocity dispersion of Sagittarius is ~ 20 km s^{-1}. Thus, parabolic encounters between GCs would be rare, but not impossible. Sagittarius does have a nuclear cluster. With a velocity dispersion of ~ 20 km s^{-1}, Sagittarius has a mass

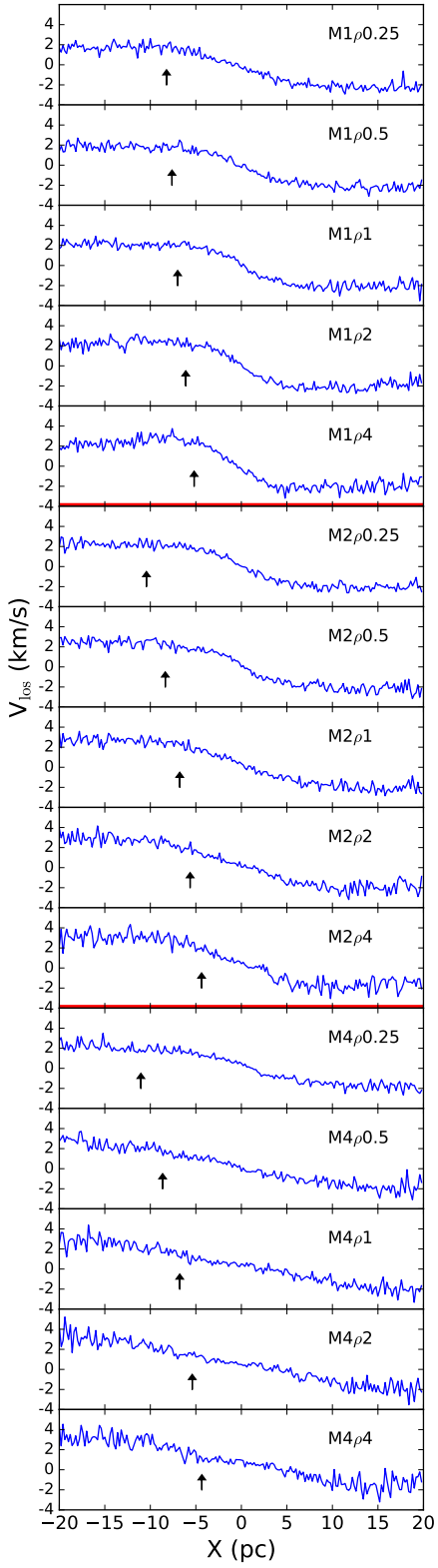

Figure 7. Line-of-sight velocity profile for all the simulations for an observer in the mid plane ($V_{\rm los}$). The half-mass radius is denoted by an arrow in each plot. The thicker red horizontal lines divide the panels by mass-ratio (the top group has $M_1/M_2 = 1$, the central $M_1/M_2 = 2$, the bottom one $M_1/M_2 = 4$). Every group has plots for the 5 density ratios considered.

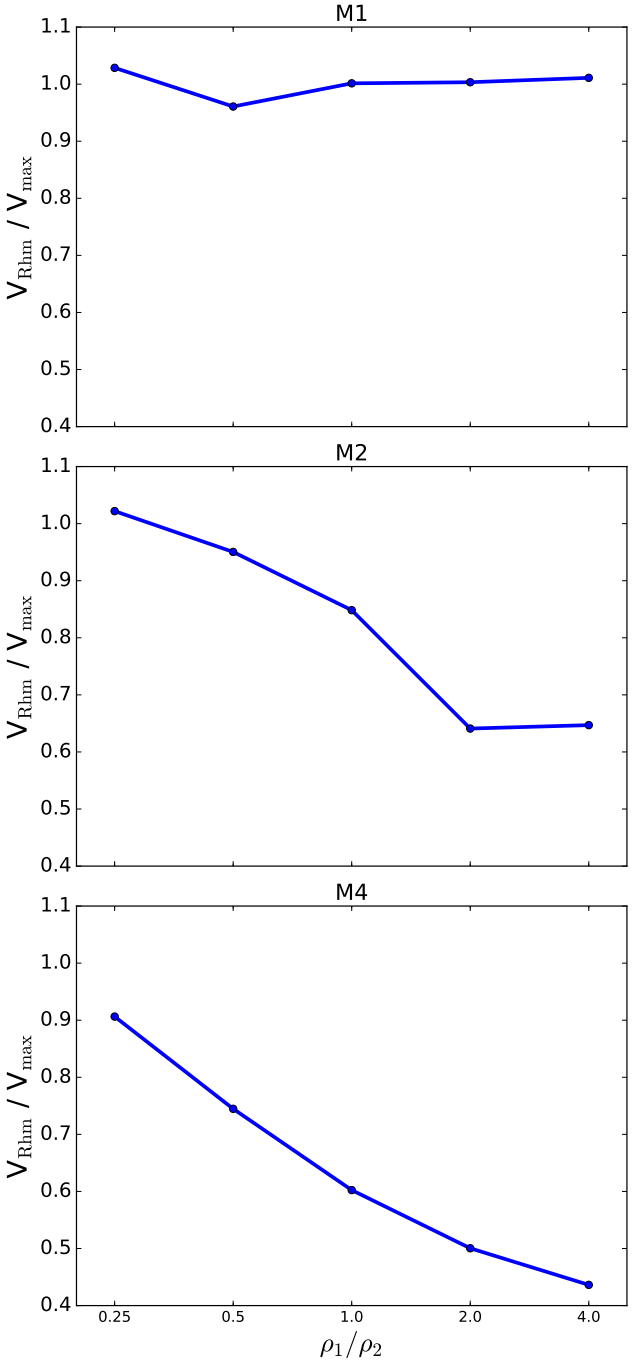

Figure 8. Ratio of the rotation velocity at the half-mass radius to the maximum rotation velocity, $V_{\rm Rhm}/V_{\rm max}$, as a function of density ratio. From top to bottom: each panel refers to GCs with mass ratio $M_1/M_2 = 1$, 2 and 4. Note that the $x-$axis is effectively logarithmic.

of $2 \times 10^8\,{\rm M}_\odot$ within one kpc, so another cluster could inspiral. Most dwarf galaxies have likely dissolved in the old stellar halo of our Galaxy. At $z = 1$, there were roughly three times as many dwarf satellites as today (Kazantzidis et al. 2008). So, there is some chance that several GCs merged within dwarf galaxies in the past. Quantifying the rate of such mergers is beyond the aims of this paper.

Finally, it is possible that two GCs merge slightly after

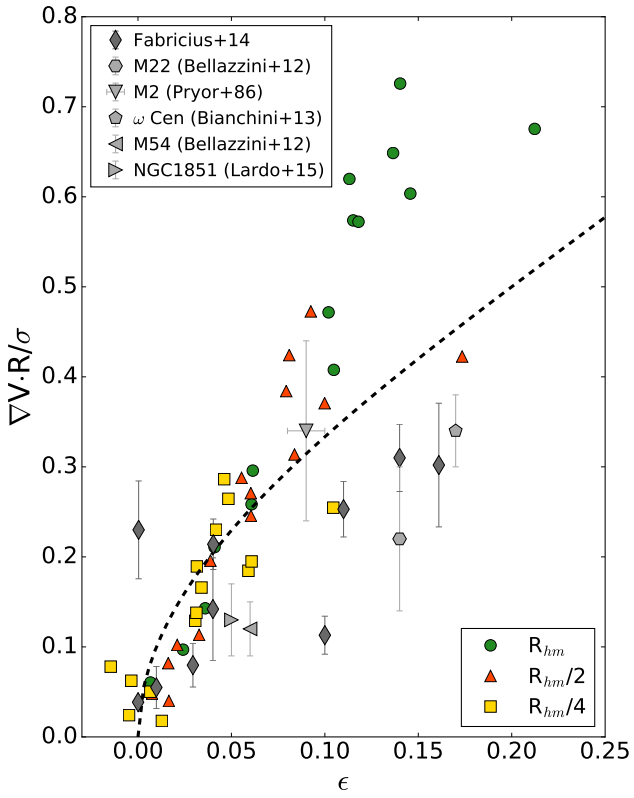

Figure 9. $(\nabla V \cdot R/\sigma,\ \varepsilon)$ for each model at different values of R. The observational points (grey) are indicated in legend in the top-left corner. The black dashed line indicates the behaviour of an isotropic oblate rotator.

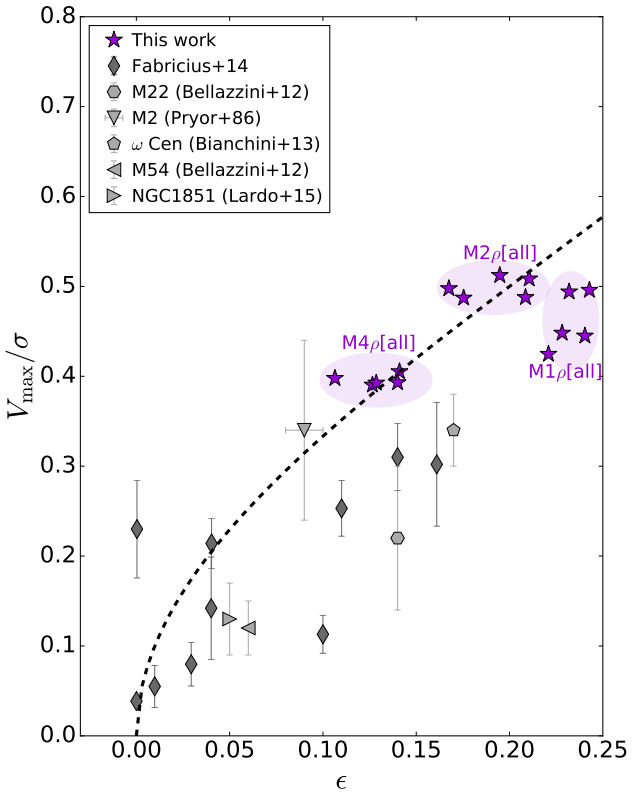

Figure 10. $(V/\sigma,\ \varepsilon)$ diagram. The purple stars refer to this work, using the maximum rotation velocity ($V_{\rm max}$) for V. The observational points (grey) are indicated in the legend. The dashed black line shows the behaviour of isotropic oblate rotators.

their formation, when they are still part of the same progenitor molecular cloud. In this case, their relative velocity should be of the same order of magnitude as the turbulent motions inside the cloud (approximately few km s^{-1}), enabling a successful merger. There are clusters younger than 100 Myr that are believed to be "caught in the act" of merging while they are still within the parent cloud (Sabbi et al. 2012).

In summary, we confirm that the merger scenario may provide a viable explanation for multiple populations in iron-complex GCs. Our simulations show that the relative concentration in the merger remnant betrays the initial density ratio of the progenitors. Moreover, the density ratio of the progenitors leaves a signature in the rotation curves that should be object of further observations.

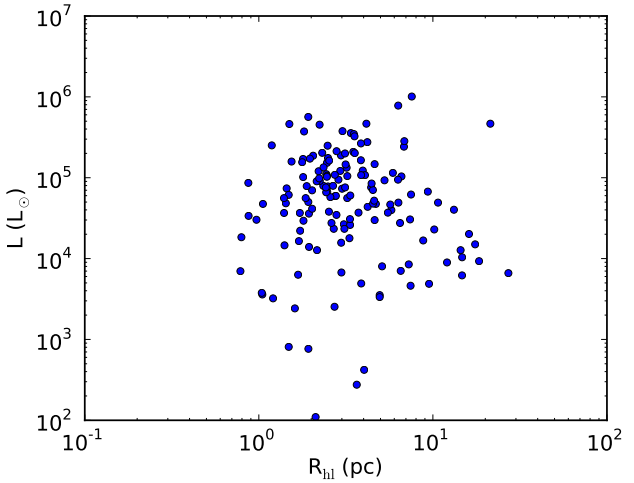

Figure 11. Total luminosity versus half-light radius of Milky Way GCs from Harris (1996)

ACKNOWLEDGEMENTS

We thank the anonymous referee for their critical reading of the manuscript and for their comments, which helped us improving this work significantly. We thank Kim Venn, Giacomo Beccari, Eugenio Carretta and Raffaele Gratton for useful discussions. The simulations were performed with the Tasna GPUs cluster of ZBOX4 at University Zurich, PLX and Eurora clusters at CINECA (through CINECA Award N. HP10B338N6 and HP10CZVZHA). We acknowledge the CINECA Award N. HP10B338N6, HP10CZVZHA and the University of Zurich for the availability of high performance computing resources. EG acknowledges financial support through SNF grant and Foundation MERAC 2014 Travel grant. MM acknowledges financial support from the Italian Ministry of Education, University and Research (MIUR) through grant FIRB 2012 RBFR12PM1F, from

INAF through grant PRIN-2014-14 (Star formation and evolution in galactic nuclei) and from Foundation MERAC through grant 'The physics of gas and protoplanetary discs in the Galactic centre'.

REFERENCES

Alladin S. M., 1965, ApJ, 141, 768
Amaro-Seoane P., Konstantinidis S., Brem P., Catelan M., 2013, MNRAS, 435, 809
Anderson A. J., 1997, PhD thesis, UNIVERSITY OF CALIFORNIA, BERKELEY
Anderson J., King I. R., 2003, AJ, 126, 772
Anderson J., Piotto G., King I. R., Bedin L. R., Guhathakurta P., 2009, ApJ, 697, L58
Bastian N., Lamers H. J. G. L. M., de Mink S. E., Longmore S. N., Goodwin S. P., Gieles M., 2013, MNRAS, 436, 2398
Bekki K., Yong D., 2012, MNRAS, 419, 2063
Bellazzini M., et al., 2008, AJ, 136, 1147
Bellazzini M., Bragaglia A., Carretta E., Gratton R. G., Lucatello S., Catanzaro G., Leone F., 2012, A&A, 538, A18
Bellini A., Piotto G., Bedin L. R., King I. R., Anderson J., Milone A. P., Momany Y., 2009, A&A, 507, 1393
Bellini A., Bedin L. R., Piotto G., Milone A. P., Marino A. F., Villanova S., 2010, AJ, 140, 631
Bertin G., Varri A. L., 2008, ApJ, 689, 1005
Bianchini P., Varri A. L., Bertin G., Zocchi A., 2013, ApJ, 772, 67
Bianchini P., Renaud F., Gieles M., Varri A. L., 2015, MNRAS, 447, L40
Binney J., 1978, MNRAS, 183, 501
Binney J., Tremaine S., 2008, Galactic Dynamics: Second Edition. Princeton University Press
Canon R.-D., Stobie R.-S., 1973, MNRAS, 162, 207
Carraro G., Lia C., 2000, A&A, 357, 977
Carretta E., 2015, preprint, (arXiv:1510.00507)
Carretta E., et al., 2007, A&A, 464, 967
Carretta E., et al., 2009a, A&A, 505, 117
Carretta E., Bragaglia A., Gratton R., Lucatello S., 2009b, A&A, 505, 139
Carretta E., Bragaglia A., Gratton R. G., Recio-Blanco A., Lucatello S., D'Orazi V., Cassisi S., 2010a, A&A, 516, A55
Carretta E., et al., 2010b, A&A, 520, A95
Carretta E., et al., 2010c, ApJ, 722, L1
Carretta E., Lucatello S., Gratton R. G., Bragaglia A., D'Orazi V., 2011, A&A, 533, A69
Chandrasekhar S., 1969, Ellipsoidal figures of equilibrium
Chandrasekhar S., Lebovitz N. R., 1962, ApJ, 136, 1037
Chen C. W., Chen W. P., 2010, ApJ, 721, 1790
Chernoff D. F., Weinberg M. D., 1990, ApJ, 351, 121
Cohen J. G., 1978, ApJ, 223, 487
D'Ercole A., Vesperini E., D'Antona F., McMillan S. L. W., Recchi S., 2008, MNRAS, 391, 825
D'Orazi V., Gratton R. G., Pancino E., Bragaglia A., Carretta E., Lucatello S., Sneden C., 2011, A&A, 534, A29
Da Costa G. S., Held E. V., Saviane I., 2014, MNRAS, 438, 3507
De Marchi G., Panagia N., Guarcello M. G., Bonito R., 2013, MNRAS, 435, 3058
Decressin T., Meynet G., Charbonnel C., Prantzos N., Ekström S., 2007, A&A, 464, 1029
Emsellem E., et al., 2007, MNRAS, 379, 401
Fabricius M. H., et al., 2014, ApJ, 787, L26
Fall S. M., Frenk C. S., 1985, in Goodman J., Hut P., eds, IAU Symposium Vol. 113, Dynamics of Star Clusters. pp 285–296
Ferraro F. R., et al., 2009, Nature, 462, 483
Freeman K.-C., Rodgers A.-W., 1975, ApJ, 201, L71
Gaburov E., Harfst S., Portegies Zwart S., 2009, New Astron., 14, 630
Geyer E. H., 1967, Z. Astrophys., 66, 16
Gieles M., 2013, in Pugliese G., de Koter A., Wijburg M., eds, Astronomical Society of the Pacific Conference Series Vol. 470, 370 Years of Astronomy in Utrecht. p. 339 (arXiv:1209.2071)
Gratton R. G., et al., 2001, A&A, 369, 87
Gratton R., Sneden C., Carretta E., 2004, ARA&A, 42, 385
Gratton R. G., Carretta E., Bragaglia A., 2012, A&ARv, 20, 50
Harris W. E., 1974, ApJ, 192, L161
Harris W. E., 1996, AJ, 112, 1487
Hesser J. E., Bell R. A., 1980, ApJ, 238, L149
Hesser J. E., Hartwick F. D. A., McClure R. D., 1977, ApJS, 33, 471
Johnson C. I., Rich R. M., Pilachowski C. A., Caldwell N., Mateo M., Bailey III J. I., Crane J. D., 2015, AJ, 150, 63
Kayser A., Hilker M., Grebel E. K., Willemsen P. G., 2008, A&A, 486, 437
Kazantzidis S., Bullock J. S., Zentner A. R., Kravtsov A. V., Moustakas L. A., 2008, ApJ, 688, 254
Kimmig B., Seth A., Ivans I. I., Strader J., Caldwell N., Anderton T., Gregersen D., 2015, AJ, 149, 53
King I. R., 1966, AJ, 71, 64
Kraft R. P., Sneden C., Langer G. E., Prosser C. F., 1992, AJ, 104, 645
Kruijssen J. M. D., 2014, Classical and Quantum Gravity, 31, 244006
Lardo C., et al., 2013, MNRAS, 433, 1941
Lardo C., et al., 2015, A&A, 573, A115
Larsen S. S., Brodie J. P., Strader J., 2012, A&A, 546, A53
Law D. R., Majewski S. R., 2010, ApJ, 718, 1128
Lee J.-W., 2015, ApJS, 219, 7
Lee Y.-W., Joo J.-M., Sohn Y.-J., Rey S.-C., Lee H.-C., Walker A. R., 1999, Nature, 402, 55
Lightman A. P., Shapiro S. L., 1978, Reviews of Modern Physics, 50, 437
Lynden-Bell D., 1967, MNRAS, 136, 101
Majewski S. R., Patterson R. J., Dinescu D. I., Johnson W. Y., Ostheimer J. C., Kunkel W. E., Palma C., 2000, in Noels A., Magain P., Caro D., Jehin E., Parmentier G., Thoul A. A., eds, Liege International Astrophysical Colloquia Vol. 35, Liege International Astrophysical Colloquia. p. 619 (arXiv:astro-ph/9910278)
Makino J., Akiyama K., Sugimoto D., 1991, Ap&SS, 185, 63
Mapelli M., Bressan A., 2013, MNRAS, 430, 3120
Mapelli M., Zampieri L., Ripamonti E., Bressan A., 2013, MNRAS, 429, 2298
Marino A. F., Milone A. P., Piotto G., Villanova S., Bedin L. R., Bellini A., Renzini A., 2009, A&A, 505, 1099
Marino A. F., et al., 2015, MNRAS, 450, 815
Massari D., et al., 2014, ApJ, 795, 22
Mastrobuono-Battisti A., Perets H. B., 2013, ApJ, 779, 85
Meylan G., Mayor M., 1986, A&A, 166, 122
Milone A. P., Piotto G., Bedin L. R., Sarajedini A., 2008, Mem. Soc. Astron. Italiana, 79, 623
Milone A. P., Stetson P. B., Piotto G., Bedin L. R., Anderson J., Cassisi S., Salaris M., 2009, A&A, 503, 755
Milone A. P., et al., 2010, ApJ, 709, 1183
Milone A. P., Marino A. F., Piotto G., Bedin L. R., Anderson J., Aparicio A., Cassisi S., Rich R. M., 2012, ApJ, 745, 27
Milone A. P., et al., 2013, ApJ, 767, 120
Milone A. P., et al., 2015, MNRAS, 447, 927
Mucciarelli A., Lapenna E., Massari D., Pancino E., Stetson P. B., Ferraro F. R., Lanzoni B., Lardo C., 2015, ApJ, 809, 128
Nataf D. M., Gould A. P., Pinsonneault M. H., Udalski A., 2013, ApJ, 766, 77
Norris J. E., Da Costa G. S., 1995, ApJ, 447, 680

Pancino E., Ferraro F. R., Bellazzini M., Piotto G., Zoccali M., 2000, ApJ, 534, L83
Pancino E., Galfo A., Ferraro F. R., Bellazzini M., 2007, ApJ, 661, L155
Pancino E., Rejkuba M., Zoccali M., Carrera R., 2010, A&A, 524, A44
Pancino E., Mucciarelli A., Sbordone L., Bellazzini M., Pasquini L., Monaco L., Ferraro F. R., 2011, A&A, 527, A18
Pasquato M., Chung C., 2016, preprint, (arXiv:1602.00993)
Peterson R. C., 1980, ApJ, 237, L87
Piotto G., et al., 2012, ApJ, 760, 39
Portegies Zwart S. F., McMillan S. L. W., Hut P., Makino J., 2001, MNRAS, 321, 199
Pryor C., Hartwick F. D. A., McClure R. D., Fletcher J. M., Kormendy J., 1986, AJ, 91, 546
Read J. I., Goerdt T., Moore B., Pontzen A. P., Stadel J., Lake G., 2006, MNRAS, 373, 1451
Renzini A., 2008, MNRAS, 391, 354
Roberts P. H., 1962, ApJ, 136, 1108
Sabbi E., et al., 2012, ApJ, 754, L37
Sarajedini A., Layden A. C., 1995, AJ, 109, 1086
Saviane I., da Costa G. S., Held E. V., Sommariva V., Gullieuszik M., Barbuy B., Ortolani S., 2012, A&A, 540, A27
Sippel A. C., Hurley J. R., Madrid J. P., Harris W. E., 2012, MNRAS, 427, 167
Sneden C., Kraft R. P., Prosser C. F., Langer G. E., 1991, AJ, 102, 2001
Spitzer L., 1987, Dynamical evolution of globular clusters
Sugimoto D., Makino J., 1989, PASJ, 41, 1117
Trani A. A., Mapelli M., Bressan A., 2014, MNRAS, 445, 1967
Varri A. L., Bertin G., 2012, A&A, 540, A94
Vesperini E., Varri A. L., McMillan S. L. W., Zepf S. E., 2014, MNRAS, 443, L79
Villanova S., Geisler D., Gratton R. G., Cassisi S., 2014, ApJ, 791, 107
White S. D. M., 1978, MNRAS, 184, 185
White R. E., Shawl S. J., 1987, ApJ, 317, 246
Yong D., Grundahl F., 2008, ApJ, 672, L29
van den Bergh S., 1996, ApJ, 471, L31
van den Bergh S., 2008, AJ, 135, 1731
van den Bosch R., de Zeeuw T., Gebhardt K., Noyola E., van de Ven G., 2006, ApJ, 641, 852

This paper has been typeset from a TEX/LATEX file prepared by the author.